K. F. Tee
Department of Aerospace Engineering,
University of Bristol,
Bristol BS8 1TR, UK

A. Spadoni
Aerospace,
California Institute of Technology,
MC 105–50,
Pasadena, CA 91125

F. Scarpa[1]
Department of Aerospace Engineering,
University of Bristol,
Bristol BS8 1TR, UK
e-mail: f.scarpa@bristol.ac.uk

M. Ruzzene
School of Aerospace Engineering,
Georgia Institute of Technology,
Ferst Drive,
Atlanta, GA

Wave Propagation in Auxetic Tetrachiral Honeycombs

This paper describes a numerical and experimental investigation on the flexural wave propagation properties of a novel class of negative Poisson's ratio honeycombs with tetrachiral topology. Tetrachiral honeycombs are structures defined by cylinders connected by four tangent ligaments, leading to a negative Poisson's ratio (auxetic) behavior in the plane due to combined cylinder rotation and bending of the ribs. A Bloch wave approach is applied to the representative unit cell of the honeycomb to calculate the dispersion characteristics and phase constant surfaces varying the geometric parameters of the unit cell. The modal density of the tetrachiral lattice and of a sandwich panel having the tetrachiral as core is extracted from the integration of the phase constant surfaces, and compared with the experimental ones obtained from measurements using scanning laser vibrometers. [DOI: 10.1115/1.4000785]

1 Introduction

Since the end of the 1940s, honeycomb and sandwich structures have seen a widespread use in aerospace and maritime constructions, due to their high stiffness to weight ratio and energy absorption characteristics under static and dynamic impact loading [1]. Cellular lattices are also extensively used in space and satellite antennas, and a consistent amount of research has been devolved to the investigation of modal density behavior of sandwich panels linked to its wave propagation properties in aerospace launchers and components, to enhance the vibroacoustic signature and structural integrity of the structures under significant dynamic loading [2]. Incidentally, the phononics community has also started to evaluate grid-like artificial periodic arrangements of inclusions and cellular structures [3–6] to develop novel sound management materials, where pass-stop bands characteristics of elastic waves can be used to selective noise filtering capabilities [4]. The work on cellular topologies for 2D in-plane and flexural wave propagation has been undertaken as a specific subset of the general wave propagation investigation on periodic structures, where regular tessellation of beams, trusses, and plates were analyzed for civil constructions and aerospace applications [6,7].

The concept of a chiral topology was first proposed at molecular level by Wojciechowski [8], and then as structural lattice component with a Poisson's ratio -1 by Prall and Lakes [9]. Chiral honeycombs are a subset of cellular solids featuring in-plane negative Poisson's ratio (or auxetic) behavior. The auxetic behavior is used to describe a material that expands laterally when stretched, or conversely contracts laterally when compressed. The unusual negative Poisson's ratio in cellular materials, in the form of honeycombs, foams, and microporous polymers [10], can be attributed to three aspects: the presence of rotational degrees of freedom, nonaffine deformation kinematics, or anisotropy [11]. A typical chiral configuration would have unit cells composed by a central cylinder, with tangent ligaments connecting cylinders from neighboring cells. When subjected to in-plane loading, the cylinders would rotate, leading to winding/unwinding of the ligaments, and therefore providing the negative Poisson's ratio effect. Most of the chiral configurations currently considered in open literature are the hexachiral ones—each cylinder being connected by six tangent ligaments [8,9]. Hexachiral cellular structures compressed under flatwise loading have demonstrated enhanced buckling strength, also compared with regular hexagonal honeycombs [12,13]. Hexachiral lattices have also shown rotational-type directionality of in-plane and flexural waves, to be used for acoustic filtering [14] and boundary layer control of cellular wingbox under dynamic loading [15]. Wave directionality and band-gap properties in phonic hexagonal chiral lattices have been also investigated with the use of the Bloch wave theorem [16].

Recently, different chiral tessellations have been proposed, almost all leading to the in-plane negative Poisson's ratio [17]. The tetrachiral lattice is one of these specific chiral topologies, where the cylinder is connected by four tangent ligaments (Fig. 1). The tetrachiral topology can also be tessellated to provide a centersymmetric configuration (antitetrachiral)—the whole honeycomb would be constructed simply by translation of the unit cell in the various directions, rather than combined rotations and translations along the tangent directions only [17]. Similarly, to hexachiral configurations, tetrachiral lattice topologies are auxetic in the plane, with a Poisson's ratio of -1 given by the bending deformation of the connected ligaments.

The current work describes for the first time the flexural wave propagation characteristics of tetrachiral honeycombs from a numerical and experimental point of view. The pass-stop band characteristics are determined through the calculations of phase constant surfaces determined using a Bloch wave approach [18] implemented in a finite element (FE) framework [19], while modal properties and modal densities of these cellular lattices are also identified experimentally and compared with the numerical simulations. A tetrachiral honeycomb panel, and a sandwich plate made of quasi-isotropic face skins and the tetrachiral lattice as core constitute the test cases. The sandwich lattice structure is simulated and tested to evaluate the possible use of these cellular phononics as cores for sandwich panels to be used in harsh vibroacoustic environments. From a design point of view, the pass-stop band characteristics of the tetrachiral lattice can easily be tuned, due to the sensitivity of the phase constant surfaces to the

[1]Corresponding author.

Contributed by the Technical Committee on Vibration and Sound of ASME for publication in the JOURNAL OF VIBRATION AND ACOUSTICS. Manuscript received March 11, 2009; final manuscript received November 10, 2009; published online April 22, 2010. Assoc. Editor: Jean-Claude Golinval.

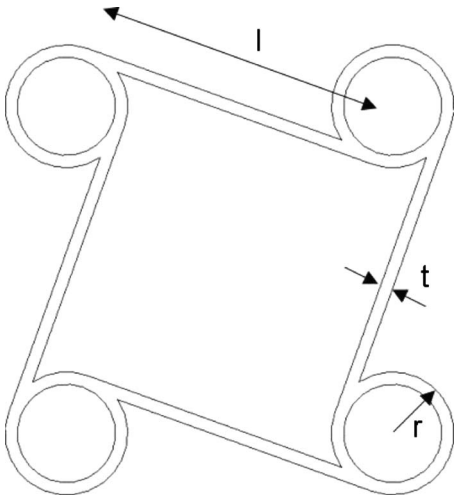

Fig. 1 Tetrachiral unit cell with representative geometric parameters

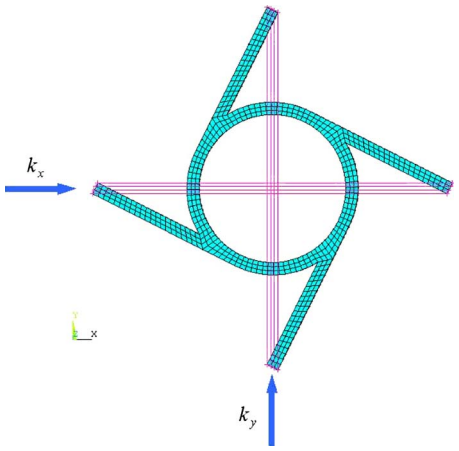

Fig. 2 Representative finite element unit cell for Bloch wave conditions

geometric parameters of the unit cells, which is investigated via a parametric analysis using the Bloch wave FE models.

2 Modeling and Testing

2.1 Geometry and the Bloch Wave Method. The structural layout of a tetrachiral honeycomb, shown in Fig. 1, consists of cylinders of radius R, acting as nodes, connected by ribs or ligaments, of length L tangent to the nodes themselves. The thickness of the node and rib walls is described by the parameter t, while the gauge thickness (height) of the honeycomb structure in the z-direction is defined as b. The following geometric relationships hold:

$$\alpha = \frac{L}{R}, \quad \beta = \frac{t}{R}, \quad \gamma = \frac{b}{R} \tag{1}$$

Tetrachiral configurations can have two separate tessellations—the conventional one shown in Fig. 1, and the antitetrachiral [17], where circular nodes are connected back to back, generating a centersymmetric structure. In this work, only the classical tetrachiral tessellation is considered.

The propagation of flexural waves in the tetrachiral honeycomb structures is investigated using a Bloch wave approach for harmonic propagating waves [18,19]. The governing equations for a homogeneous anisotropic body with linear elastic properties are

$$\sigma_{ij,j} = \rho \frac{\partial^2 u_i}{\partial t^2}, \quad \sigma_{ij,j} = C_{ijkl}\varepsilon_{kl}, \quad \varepsilon_{kl} = \frac{1}{2}(u_{k,l} + u_{l,k}) \tag{2}$$

The solution for generalized displacements can be assumed as the following:

$$u_m(x_n,t) = U_m(x_n)e^{-i\omega t} \tag{3}$$

Using Eq. (3), the stress and strain tensors of the body become complex functions of the type

$$\sigma_{ij}(x_n,t) = \Sigma_{ij}(x_n)e^{-i\omega t}, \quad \varepsilon_{ij}(x_n,t) = E_{ij}(x_n)e^{-i\omega t} \tag{4}$$

Substituting Eqs. (3) and (4) in Eq. (2), the new governing equations of motion become

$$\Sigma_{ij,j} + \rho\omega^2 U_i = 0, \quad \Sigma_{ij} = C_{ijkl}E_{kl}, \quad E_{kl} = \tfrac{1}{2}(U_{k,l} + U_{l,k}) \tag{5}$$

Using Bloch's theorem, the complex generalized displacements on a periodic unit cell (Fig. 2) can be expressed as

$$U_m(x_n,t) = U_m(x_n + l_n)e^{-ikn_j l_j} \tag{6}$$

The degrees of freedom (DOFs) of a centersymmetric unit cell can be decomposed into left (L), right (R), top (T), and bottom (B) (Fig. 2). The Floquet conditions for wave propagation in a Cartesian xy coordinates frame are the following:

$$U_B = U_T e^{-ik_y y}, \quad U_L = U_R e^{-ik_x x} \tag{7}$$

Because of the complex terms, Eq. (6) can be decomposed as

$$U_m(x_n) = U_m^{\mathrm{Re}}(x_n) + iU_m^{\mathrm{Im}}(x_n) \tag{8}$$

Imposing Eq. (8) in the second of Eq. (2), the new equations of motion become

$$\Sigma_{ij,j}^{\mathrm{Re}} + \rho\omega^2 U_i^{\mathrm{Re}} = 0 \tag{9a}$$

$$\Sigma_{ij,j}^{\mathrm{Im}} + \rho\omega^2 U_i^{\mathrm{Im}} = 0 \tag{9b}$$

The implementation of Eq. (8) in a finite element implicit method leads to the creation of two superimposed meshes, one corresponding to the real part and the other to the imaginary part. The connection between the boundary DOFs of the two meshes is performed using the following periodic boundary conditions:

$$U_1^{\mathrm{Re}} = U_2^{\mathrm{Re}} \cos(kn_j l_j) + U_2^{\mathrm{Im}} \sin(kn_j l_j) \tag{10a}$$

$$U_1^{\mathrm{Im}} = U_2^{\mathrm{Im}} \cos(kn_j l_j) - U_2^{\mathrm{Re}} \sin(kn_j l_j) \tag{10b}$$

where $kn_j l_j$ are the propagation constants of the wave vector. Considering the first Brillouin zone $-\pi \le k_x, k_y \le \pi$, the Eq. (10) can be rewritten in terms of the x and y components of the wave vector

$$U_{\mathrm{bottom}}^{\mathrm{Re}} = U_{\mathrm{top}}^{\mathrm{Re}} \cos(k_y) + U_{\mathrm{top}}^{\mathrm{Im}} \sin(k_y) \tag{11}$$

$$U_{\mathrm{left}}^{\mathrm{Im}} = U_{\mathrm{right}}^{\mathrm{Im}} \cos(k_x) - U_{\mathrm{right}}^{\mathrm{Re}} \sin(k_x) \tag{12}$$

$$U_{\mathrm{left}}^{\mathrm{Re}} = U_{\mathrm{right}}^{\mathrm{Re}} \cos(k_x) + U_{\mathrm{right}}^{\mathrm{Im}} \sin(k_x) \tag{13}$$

$$U_{\mathrm{bottom}}^{\mathrm{Im}} = U_{\mathrm{top}}^{\mathrm{Im}} \cos(k_y) - U_{\mathrm{top}}^{\mathrm{Re}} \sin(k_y) \tag{14}$$

The finite element models can therefore be coupled using the Eqs. (11)–(14). For a given set of k_x and k_y, the eigenvalues of Eq. (9) can be calculated using a BLOCK LANCZOS algorithm. The solutions of the eigenvalue problem constitute the phase constant surfaces of the periodic structure, providing information on the stop-pass bands of the honeycomb. The total number of modes N less than a specified frequency ω_0 for a structural lattice panel made of N_1, N_2 cells in the x and y directions can be derived from the following [20]:

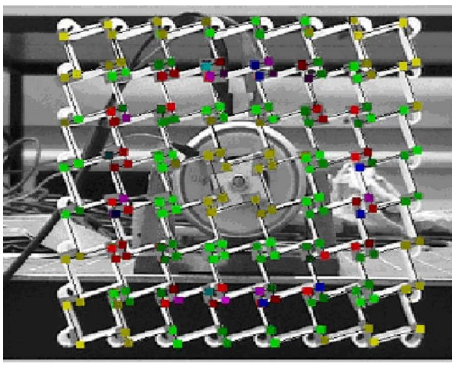

(*a*)

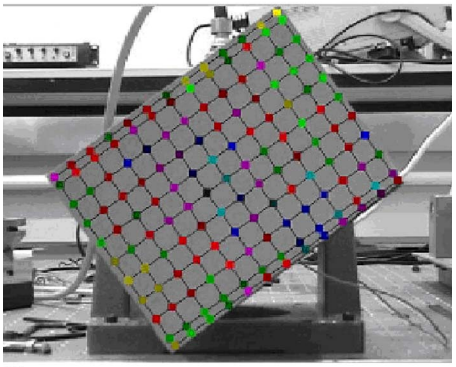

(*b*)

Fig. 3 (*a*) RP tetrachiral lattice panel mounted on electrodynamic shaker and (*b*) flat sandwich tetrachiral lattice mounted on the same rig

$$N = \frac{N_1 N_2}{\pi^2} \int \int_{f(k_x,k_y)<\omega_0} dk_x dk_y \tag{15}$$

where $f(k_x,k_y)$ is a phase constant surface. The modal density for a single phase constant surface can be estimated numerically as

$$n = \frac{\partial N}{\partial \omega_0} \tag{16}$$

The modal density for the whole honeycomb structure can be evaluated by summing Eq. (16) over each phase constant surface, which is present at this frequency.

2.2 Manufacturing and Testing. Tetrachiral honeycomb structures were manufactured using a rapid prototyping (RP) selective laser sintering (SLS) technique based on polyamide sintered powders. The aspect ratio α of the cells was 6, with a relative thickness β equal to 0.4. The length of the straight side L was 2.54 cm, with a gauge thickness b of 2.5 cm. The total honeycomb panel room was $19.5 \times 19.5 \times 2.5$ cm^3 (7×7 unit cells). The Young's modulus of the core material measured on a BSI standard sample under tensile loading was 1.6 GPa. A sandwich panel with the tetrachiral structural lattice was build using a similar core (7×5 unit cells) with 2 face quasi-isotropic composite skins made by a 8552 prepreg with a 0/−45/+45/90/90/+45/−45/0 stacking layer sequence. The face skins and the core were attached with an epoxy-resin based adhesive and cured in autoclave at 120 deg.

The wave propagation behavior of the tetrachiral honeycomb and sandwich panels (Figs. 3(*a*) and 3(*b*)) was measured using a scanning laser vibrometer (Polytec PSV-300 F). An electrodynamic shaker (Ling Dynamic Systems V406) was used to provide white noise broadband base excitation. A DSpace-based signal generator provided input to the shaker through a power amplifier (model LDS PA100E). Input force was detected using a PCB

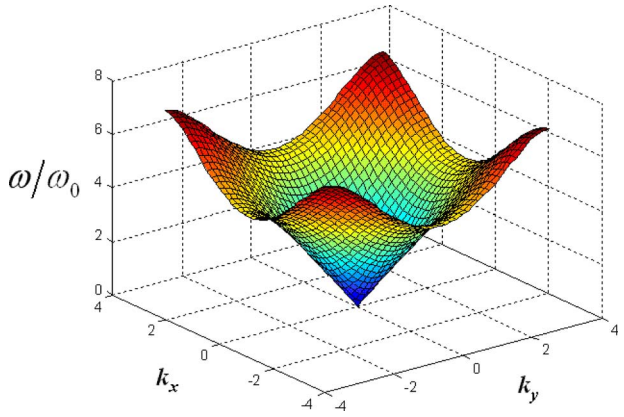

Fig. 4 First constant phase surface for tetrachiral lattice (α =6, β=0.4, γ=1)

208C03 force transducer. The resolution, force range, sensitivity, and frequency range of the force transducer are 0.005 lb (0.022 N) rms, ±500 lb (2224 N), 2.37 mV/N, and 36 kHz, respectively. The tetrachiral lattice panel was connected to the shaker using a stinger and two thin aluminum square base plates attached to the center. For the tetrachiral sandwich panel, the force transducer was connected to the panel using thin aluminum round base plate fixed on the center (Fig. 3(*b*)). The velocity range for the SLV was 1 mm/s, corresponding to a vibrometer output voltage of 1 V. A FFT acquisition was performed within a selected bandwidth between 0 kHz and 5 kHz. The SLV was used to perform a modal analysis of the tetrachiral honeycomb and sandwich panel, as well as the measurements of the modal densities of the cellular structures. For the modal analysis, the input was a random excitation, whereas 252 points on the surface of the tetrachiral honeycomb core panel were used as measurement locations, each scanning point and FFT averaged 20 times. For the tetrachiral sandwich panel, 143 points were scanned. FRFs for each data point and average FRF were obtained, and stored in a universal file for postprocessing using the LMS modal analysis software. The experimental modal densities have been derived using a modal count method [21], and from the averaged point mobility Y through [2]

$$n(f) = 4m\langle \mathrm{Re}(Y) \rangle \tag{17}$$

where m is the mass of the panel and $\langle \mathrm{Re}(Y) \rangle$ is the spatial average of the real part of the driving point admittance, which can be extracted directly from the H_1 indicator of the average spectrum [22]. Driving point admittance, Y is the ratio of the Fourier transform of the velocity of the excitation point to the Fourier transform of the excitation force, being equivalent to a FRF, which can be obtained directly from the scanning laser vibrometer. Nine different excitation point locations were used for the modal density of the tetrachiral honeycomb core panel, with the real part of the driving point admittances averaged spatially using the two-channel technique [22]. For the tetrachiral sandwich panel, one center excitation point was used instead.

3 Results and Discussions

The first phase constant surface from the eigensolution of Eq. (9) for a tetrachiral sandwich unit cell is shown in Fig. 4, for the case where only degrees of freedom along the z-direction are considered (SH waves). The phase constant surfaces are generally symmetric with respect both to the k_x and k_y axes [23]. This property can be utilized to limit the analysis of the surfaces to the first quadrant of the k_x, k_y plane, with both k_x and k_y varying in the range $0-\pi$. The results have been normalized against the fundamental frequency $\omega_0 = \bar{\omega}\pi^2/(2N_1N_2)$ [23], where ϖ corresponds to the first nonzero mode at (k_x=0, k_y=0), and N_1 and N_2 are the

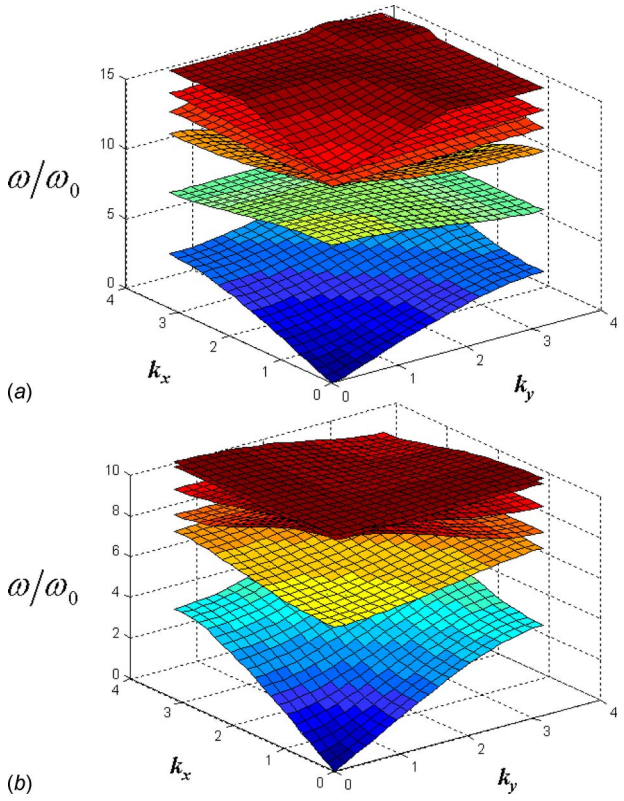

Fig. 5 Phase constant surfaces cascade for (*a*) tetrachiral lattice and (*b*) sandwich unit cells (α=6, β=0.4, γ=1)

number of cells along the x and y directions. The computed normalized frequency ω_0 for the 7×7 cells lattice panel for 253 Hz. The tessellation of the sandwich panel was composed by 5×7 unit cells, and the normalized frequency ω_0 was equal to 1724 Hz. The first six phase constant surfaces for both the tetrachiral lattice core and sandwich unit cells are shown in Figs. 5(a) and 5(b), respectively corresponding to different pass-stop bands. The phase constant surfaces are plotted with both k_x and k_y varying in the range from 0 to π for symmetry reasons. It is interesting to notice how the presence of the face skin on the honeycomb unit cells provide lower values for the last four normalized phase constant surfaces, as shown in Fig. 5(b). An important aspect when considering the wave propagation behavior in lattice cores is also the SH-type acoustic wave of shear modes. These frequencies are significantly damped due to the high constraining shearing effect given by the core and bending of the face skins. Wave modes assumed by the unit cell depend on the Poynting vector, i.e., the wavenumber components. The first four modes associated to (0,0), $(\pi,0)$ and $(\pi/4,\pi/4)$ for both tetrachiral core and sandwich unit cell are depicted in Figs. 6 and 7, respectively. The wave propagation analysis is further simplified by considering irreducible Brillouin zones [24], which are used to limit the variation in the wave vector and can be defined as the smallest area allowing full representation of the phase constant surface variation. The dispersion curves for the lowest ten modes calculated along the perimeter of the irreducible zone for the tetrachiral and sandwich lattice structures are shown in Figs. 8(a) and 8(b), respectively. For both plots, it can be noticed that one dispersion curve starts from the zero position, i.e., the system is characterized by one degree of freedom only. For the tetrachiral lattice, a stop band related to the whole irreducible zones can be identified for $7<\omega/\omega_0<8$ (Fig. 8(a)). The presence of the face plates on the tetrachiral lattice contributes to the shift of the stop bands to higher frequency ratios, with the presence of three bands for $11.5<\omega/\omega_0<12.5$,

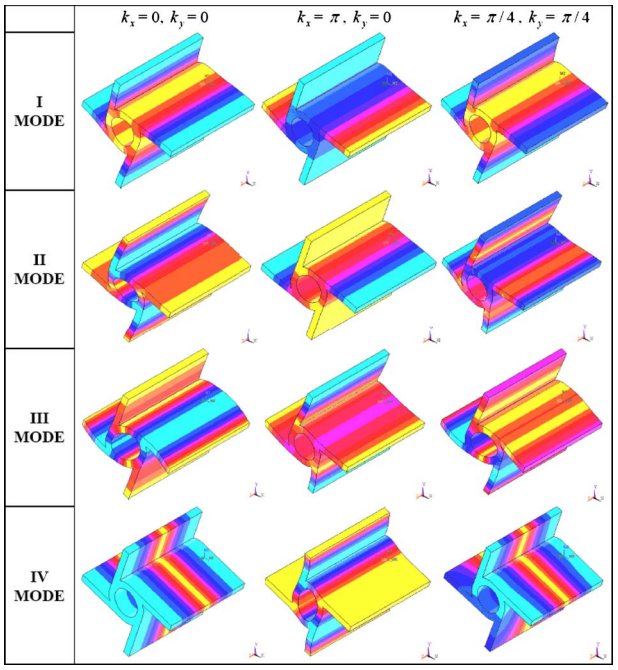

Fig. 6 First four eigenmodes of (6) for the tetrachiral lattice for different wave vector combinations

$12.8<\omega/\omega_0<13.7$, and $14.2<\omega/\omega_0<14.5$ (Fig. 8(b)). Frequency veering (i.e., convergence and divergence of the eigenvalues without crossing [25]) for both the tetrachiral lattice and sandwich panel is also evident, with the distribution of band gaps and veering close to the one of centersymmetric cellular configurations [24]. When considering a general wave propagation for the

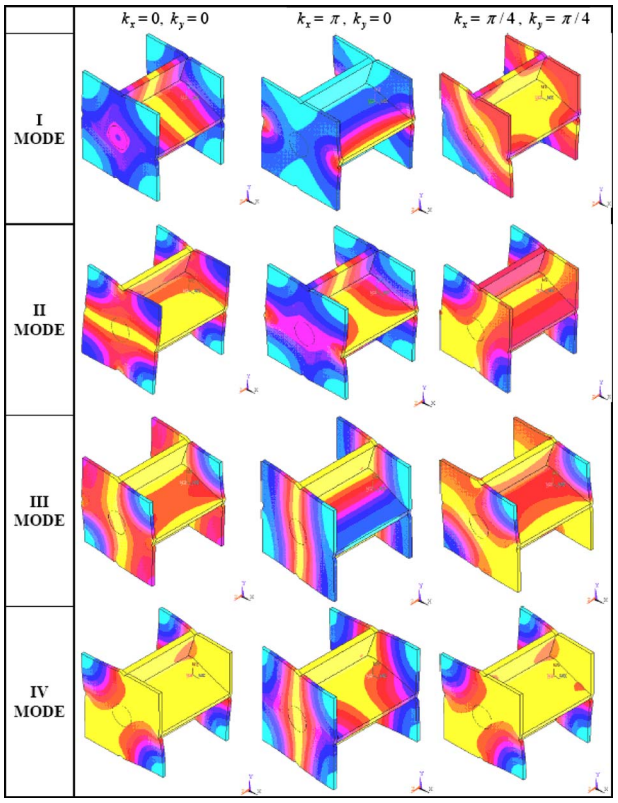

Fig. 7 First four eigenmodes of (6) for the tetrachiral sandwich for different wave vector combinations

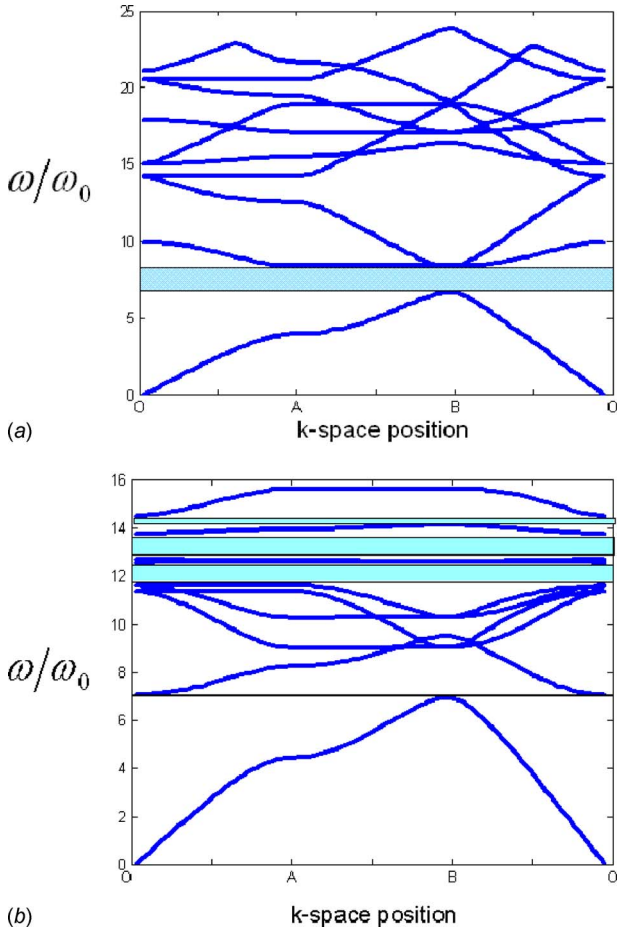

Fig. 8 Dispersion curves in the wave number vector space for (*a*) tetrachiral lattice and (*b*) sandwich unit cell. Only the displacement along the *z*-direction is allowed.

cellular system (i.e., with all the degrees of freedom of the numerical model unconstrained), the pass-stop band behavior is less evident (Fig. 9). As expected, three branches of the dispersion curves start from the origin of the irreducible zone, corresponding to the rigid body modes associated to the degrees of freedom. Strong mode veering is recorded for the for modes 2, 3, and 4 around the $(\pi\sqrt{2}/2,0)$ irreducible zone, and also for higher modes in position $(-\pi,\pi)$ in the frequency ratio $\omega/\omega_0 \sim 22$. No evident pass-stop band gap across the zones is recorded.

The lattice panel subjected to base excitation (Fig. 3(*a*)) showed global modes at 308 Hz, 570 Hz, 1020 Hz, and 1470 Hz. All the modes were flexural, apart from the third, which was a torsional one. The lattice sandwich panel (Fig. 3(*b*)) showed global modes at 1272 Hz, 1522 Hz, 2089 Hz, and 2597 Hz. The first mode was related to global torsion, while all the other mode shapes were flexural. As showed by the dispersion curves in the irreducible Brillouin space, the effect of adding face skins to the tetrachiral lattice is to move pass-stop bands at higher frequency ratio. This is further reinforced by observing the plot of the experimental average spectrum modal density (Eq. (17)) for the lattice and sandwich panel shown in Figs. 10(*a*) and 10(*b*), where the masses of the lattice and sandwich panel are 0.234 kg and 0.373 kg, respectively. The normalizing frequencies ω_0 are the first experimental natural frequencies (bending modes) for the lattice panel and sandwich structure (308 Hz and 1272 Hz, respectively). The ω_0 value simulated with the Bloch wave method for the lattice panel is 18% lower than the natural frequency associated to the first bending mode. For the sandwich panel, the Bloch wave overestimates the first experimental flexural mode by 13.2%. From Fig. 10(*a*), one can observe that the presence of the face skins tends to shift the regular distributions of the peaks related to the tetrachiral lattice average spectrum of the mobility $\dot{w}/F$ (real part), where w is the displacement of the structure along the z-direction and F the magnitude of the harmonic point force. The amplitude of the mobility is decreased with increasing frequency bandwidth, albeit the regularity of the pass-stop bands characteristics are maintained. The face skins act as high-pass filter for phase constant surfaces higher than the third of the honeycomb panel, and only highly coupled shearing-bending modes give provide contributions to significant resonant behavior. It is also worth

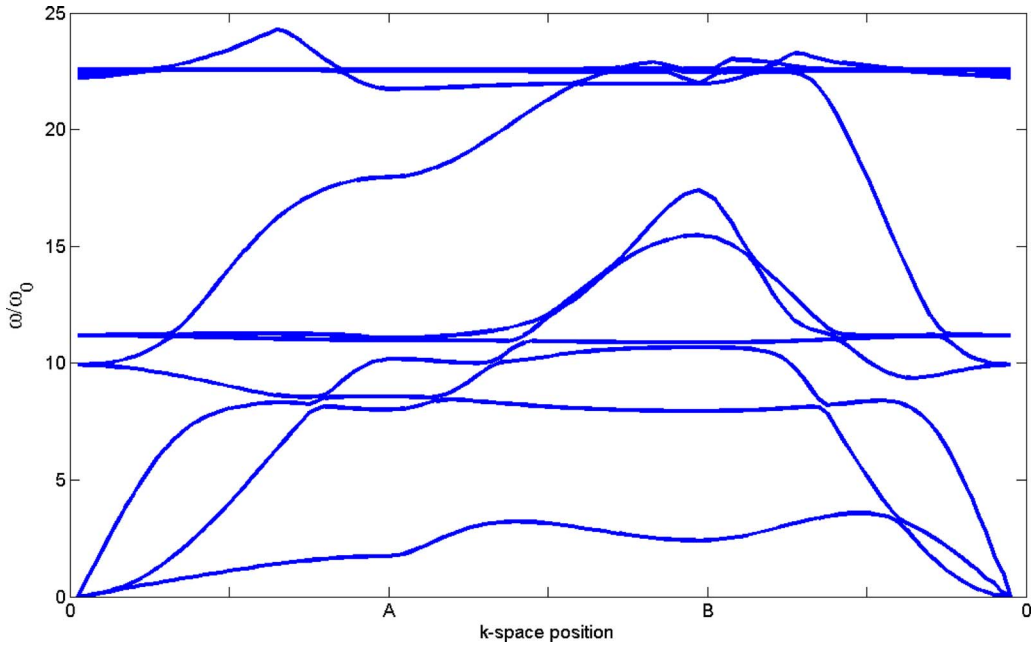

Fig. 9 Dispersion curves in the wave number vector space for the tetrachiral lattice unit cell. All degrees of freedom unconstrained.

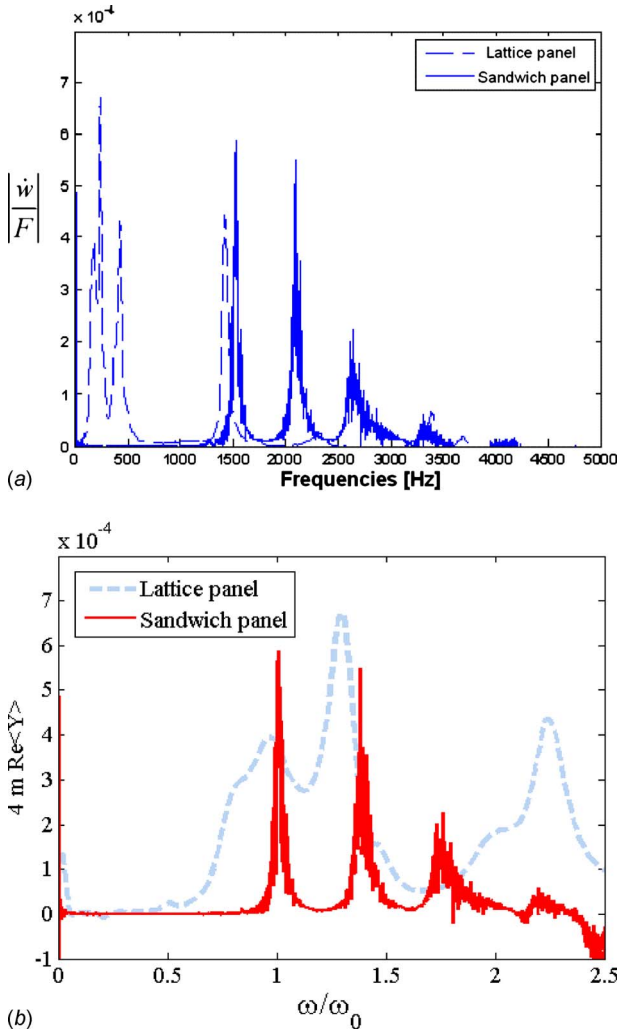

Fig. 10 Experimental spectrum of the average mobility for (*a*) tetrachiral lattice and (*b*) sandwich panel

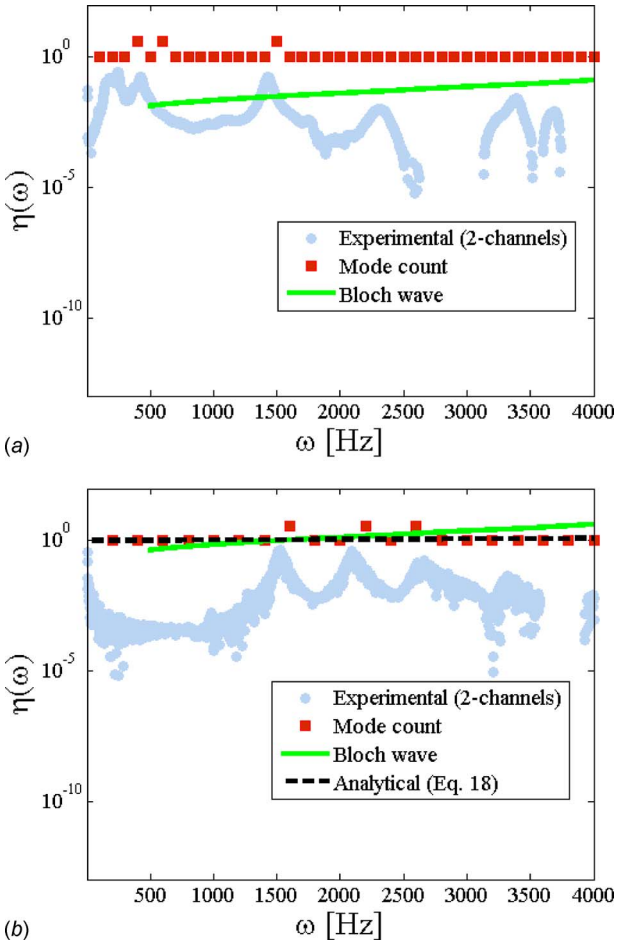

Fig. 11 Comparison between analytical, numerical, and experimental modal densities. (*a*) tetrachiral lattice and (*b*) sandwich panel.

noticing closer frequency spacing for the mobility peaks for the case of the sandwich panel, while in the nondimensional frequency range the lattice panel without skins tends to have wider spacing between peaks with broader spectrum (Fig. 10(*b*)).

A comparison between experimental and numerical modal densities obtained from the phase constant surfaces (Eq. (16)) is illustrated in Figs. 11(*a*) and 11(*b*) versus the excitation frequency. Besides the two-channel technique, mode count is also used for the comparison with the Bloch wave FE model. As confirmed by other experimental tests [22], the two-channel technique underestimates the modal density of the cellular panel compared with the mode-count approach. For the tetrachiral lattice case (Fig. 11(*a*)), there is a satisfying agreement between the experimental mode count and the numerical modal densities estimated using Eq. (16), with the concurrence between the two methods improving for increasing frequencies. For the flat sandwich panel (Fig. 11(*b*)) it is also possible to use an analytical expression for the modal density, when an isotropic core with face bending stiffness neglected and anisotropic skin is considered [26]

$$\frac{1}{(\pi/4)(a/b)}\frac{dN}{d(\omega/\omega_0)} \approx \left(1+\frac{\chi}{r}\right)\left(r\frac{\omega}{\omega_0}\right) + \frac{1+(1/2)[1-(\chi/r)]^2[r(\omega/\omega_0)]^2}{\sqrt{1+(1/4)[1-(\chi/r)]^2[r(\omega/\omega_0)]^2}} \tag{18}$$

where a and b are axial length and circumferential width of the panel, respectively, r is the shear flexibility, χ is the rotary inertia, and the frequencies are normalized with fundamental frequency ω_0. As in the case of the tetrachiral lattice, the results obtained from the two-channel technique are substantially lower when compared with the analytical (Eq. (18)), Bloch wave, and mode-count values. For the particular test rig used, the physical size of the mounting stud would affect the results [27], and a larger stud would provide a lower modal density. However, the modal densities from the Bloch wave FE model provide a very good comparison with the analytical modal densities estimated using Eq. (18), and follow the trend of the experimental mode-count results. For both cases, the comparison confirms the choice of modeling SH wave-type of motion in the Bloch wave models (i.e., only motion along the z-axis permitted). The scanning laser vibrometer can detect only structural velocities normal to the vibrating surface; therefore, only displacements and velocities normal to the plane of the unit cell should be considered.

From a parametric aspect point of view, it is interesting to understand the dependency of the eigenmodes solutions versus the geometric cell parameters of the tetrachiral configuration. In general, the compressive elastic and transverse shear modulus scale linearly with the relative density β for cellular configurations [28]. On the other end, the increase in the gauge thickness γ tends not only to increase the mass of the cell, but also to decrease the shear modulus toward the lower Reuss bound [27], providing a decrease in the magnitude of eigensolutions associated to shear mode behavior. Figures 12(*a*)–12(*c*) and 13(*a*)–13(*c*) show the sensitivity of the eigenmodes for the phase constant surfaces versus the cell

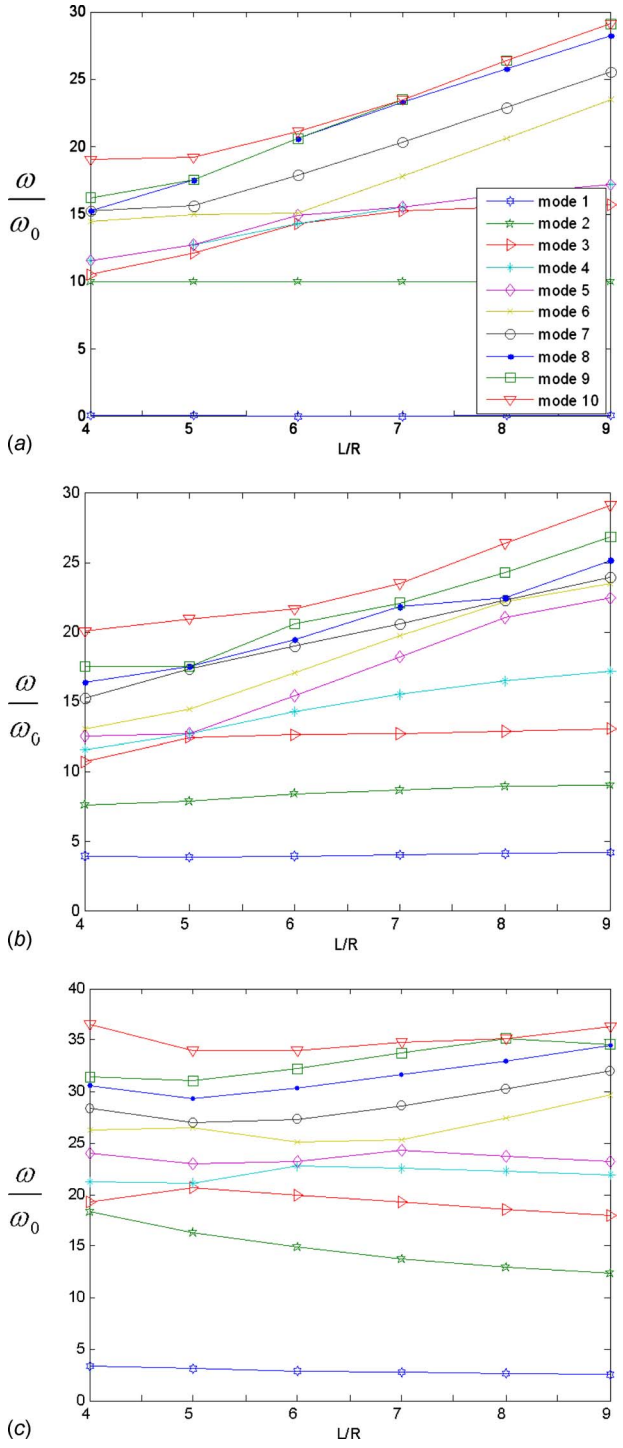

Fig. 12 Sensitivity of eigensolutions versus the cell wall aspect ratio L/R for the tetrachiral core (a) $k_x=0$, $k_y=0$; (b) $k_x=\pi$, $k_y=0$; and (c) $k_x=\pi/4$, $k_y=\pi/4$. Only the z-displacement is allowed.

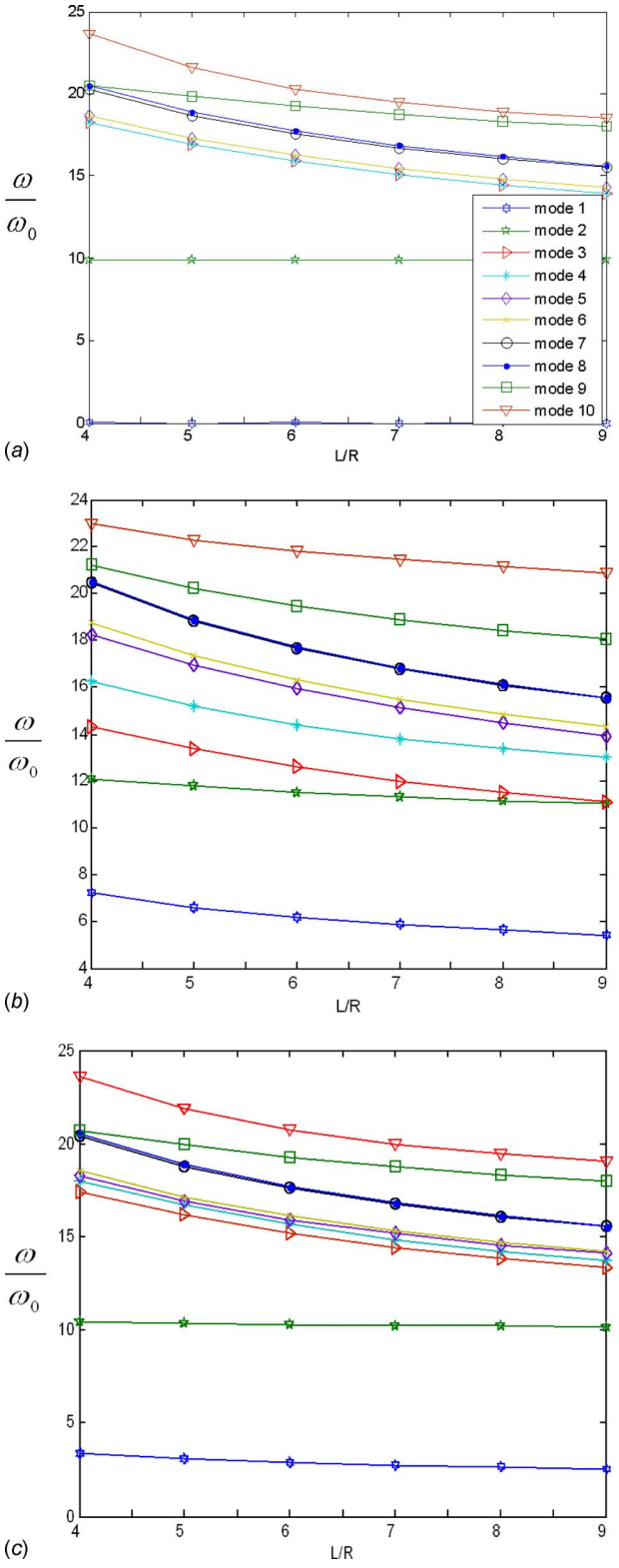

Fig. 13 Sensitivity of eigensolutions versus the cell wall aspect ratio L/R for the sandwich panel: (a) $k_x=0$, $k_y=0$; (b) $k_x=\pi$, $k_y=0$; and (c) $k_x=\pi/4$, $k_y=\pi/4$. Only the z-displacement is allowed.

aspect ratio $\alpha=L/R$ for different wavenumber combinations, for the tetrachiral lattice and sandwich panel, respectively. For the (0,0) wavenumbers combination (Fig. 12(a)), only modes higher than 2 seem affected by an increase in the cell wall aspect ratio. These modes are associated to flexural behavior of the ligaments and pure axial deformation along the z-direction (Fig. 6). Mode veering also seems to occur for four mode branches at $\alpha=6$. The modes with strong axial deformations (modes 4, 6, and 8) show a higher sensitivity versus those for the $(\pi,0)$ case (Fig. 12(b)), although all the modes seem to be affected by the increase in cell wall aspect ratio, apart for the first three. A different situation seems to occur for the case $(\pi/4,\pi/4)$ in Fig. 12(c), where the modes are combinations of flexural-shear deformations (Fig. 6),

for which the eigenvalues tend to decrease for increasing cell wall aspect ratio. For increasing α values and a given gauge thickness, the value of the transverse shear modulus for tetrachiral structural lattices tend to decrease [29]; therefore, it is likely that modes associated with strong shear coupling will provide decreasing resonances for the unit cell for increasing L/R values. This fact is also confirmed for the sensitivities of the eigensolutions for the sandwich unit cells (Fig. 13). In sandwich structures subjected to flexural waves, the face skins provide the bending stiffness as Kirschoff plates, while the contribution of the core to the bending flexibility is through the shear stiffness [26]. For increasing α values, and therefore decreasing shear stiffness of the tetrachiral lattice, the overall bending and shear flexibility of the sandwich unit is decreased, and not balanced by the decrease in the relative density of the cellular material for a fixed configuration of skin properties [12]. This appears to be valid for all wavenumber pairs considered in Figs. 13(a)–13(c), with a general trend of constant decrease for the eigensolutions of the sandwich unit element.

4 Conclusions

The tetrachiral honeycomb configuration provides a new interesting platform for novel sandwich structures with negative Poisson's ratio, where dome-shaped and sinclastic curvatures are required to manufacture complex geometries, from air ducts, fuselage components, nacelle engines, and satellite antennas. Compared with hexachiral configurations, the reduced number of ligaments (four) allow both centersymmetric and noncentersymmetric honeycomb configurations, with reduced density and easier manufacturing process to be used (RP or RTM). The overall modal density and wave propagation behavior, and therefore the acoustic signature, is strongly dependent on the geometric parameters of the unit cell (relative density and cell wall aspect ratio). This significant sensitivity versus the topology of the unit cell suggests potential use also in tuning band-gap structures, both in terms of passive design and active vibration control [30].

Acknowledgment

This work has been funded by the FP6 Project No. NMP3-CT-2005-013641—CHISMACOMB.

References

[1] Vinson, J., 1999, *The Behaviour of Sandwich Structures of Isotropic and Composite Materials*, Technomic, Lancaster, PA.
[2] Clarkson, B. L., and Pope, R. J., 1981, "Experimental Determination of Modal Densities and Loss Factors of Flat Plates and Cylinders," J. Sound Vib., **77**(4), pp. 535–549.
[3] Vasseur, J. O., Djafari-Rouhani, B., Dobrzynski, L., Kushwaha, M. S., and Halevi, P., 1994, "Complete Acoustic Band Gaps in Periodic Fibre Reinforced Composite Materials: The Carbon/Epoxy Composite and Some Metallic Systems," J. Phys.: Condens. Matter, **6**, pp. 8759–8770.
[4] Wen, J., Yu, D., Wang, G., Zhao, H., and Wen, X., 2008, "Directional Propagation Characteristics of Flexural Wave in Two-Dimensional Periodic Grid-Like Structures," J. Phys. D: Appl. Phys., **41**, p. 135505.
[5] Wen, J.-H., Yu, D.-L., Wang, G., Zhao, H.-G., Liu, Y.-Z., and Wen, X.-S., 2007, "Directional Propagation Characteristics of Flexural Waves in Two-Dimensional Thin-Plate Phononic Crystals," Chin. Phys. Lett., **24**(5), pp. 1305–1308.
[6] Yang, W. P., and Chen, L. W., 2008, "The Tunable Acoustic Band Gaps of Two-Dimensional Phononic Crystals With a Dielectric Elastomer Cylindrical Actuator," Smart Mater. Struct., **17**, p. 015011.
[7] Mead, O., 1973, "A General Theory of Harmonic Wave Propagation in Linear Periodic Systems With Multiple Coupling," J. Sound Vib., **27**, pp. 235–260.
[8] Wojciechowski, K. W., 1989, "Two-Dimensional Isotropic System With a Negative Poisson's Ratio," Phys. Lett. A, **137**, pp. 60–64.
[9] Prall, D., and Lakes, R. S., 1996, "Properties of a Chiral Honeycomb With Poisson's Ratio of −1," Int. J. Mech. Sci., **39**, pp. 305–314.
[10] Evans, K. E., and Alderson, A., 2000, "Auxetic Materials: Functional Materials and Structures From Lateral Thinking!" Adv. Mater., **12**, pp. 617–628.
[11] Lakes, R. S., 1991, "Deformation Mechanisms in Negative Poisson's Ratio Materials-Structural Aspects," J. Mater. Sci., **26**, pp. 2287–2292.
[12] Scarpa, F., Blain, S., Lew, T., Perrott, D., Ruzzene, M., and Yates, J. R., 2007, "Elastic Buckling of Hexagonal Chiral Cell Honeycombs," Composites Part A, **38**(2), pp. 280–289.
[13] Spadoni, A., Ruzzene, M., and Scarpa, F., 2005, "Global and Local Linear Buckling Behavior of a Chiral Cellular Structure," Phys. Status Solidi B, **242**(3), pp. 695–709.
[14] Spadoni, A., and Ruzzene, M., 2006, "Structural and Acoustic Behavior of Chiral Truss-Core Beams," ASME J. Vibr. Acoust., **128**, pp. 616–626.
[15] Spadoni, A., Ruzzene, M., and Scarpa, F., 2006, "Dynamic Response of Chiral Truss-Core Assemblies," J. Intell. Mater. Syst. Struct., **17**(11), pp. 941–952.
[16] Spadoni, A., Ruzzene, M., Gonella, S., and Scarpa, F., 2009, "Phononic Properties of Hexagonal Chiral Lattices," Wave Motion, **46**(7), pp. 435–450.
[17] Grima, J. N., Gatt, R., and Farrugia, P.-S., 2008, "On the Properties of Auxetic Meta-Tetrachiral Structures," Phys. Status Solidi B, **245**(3), pp. 511–520.
[18] Ruzzene, M., Scarpa, F., and Soranna, F., 2003, "Wave Beaming Effect in Bi-Dimensional Cellular Structures," Smart Mater. Struct., **12**, pp. 363–372.
[19] Åberg, M., and Gudmundson, P., 1997, "The Usage of Standard Finite Element Codes for Computation of Dispersion Relations in Materials With Periodic Microstructure," J. Acoust. Soc. Am., **102**(4), pp. 2007–2013.
[20] Langley, R. S., 1994, "On the Modal Density and Energy Flow Characteristics of Periodic Structures," J. Sound Vib., **172**(4), pp. 491–511.
[21] Renji, K., 2000, "Experimental Modal Densities of Honeycomb Sandwich Panels at High Frequencies," J. Sound Vib., **237**(1), pp. 67–79.
[22] J. M. M. Silva, N. M. M. Maia, and J. M. M. E. Silva, eds., 1997, *Theoretical and Experimental Modal Analysis*, Research, Taunton, UK.
[23] Langley, R. S., 1996, "The Response of Two-Dimensional Periodic Structures to Point Harmonic Forcing," J. Sound Vib., **197**, pp. 447–469.
[24] Srikantha Phani, A., Woodhouse, J., and Fleck, N., 2006, "Wave Propagation in Two-Dimensional Periodic Lattices," J. Acoust. Soc. Am., **119**(4), pp. 1995–2005.
[25] Perkins, N. C., and Mote, C. D. J., 1986, "Comments on Curve Veering in Eigenvalue Problems," J. Sound Vib., **106**(3), pp. 451–463.
[26] Erickson, L. L., 1970, "Modal Density Estimates for Sandwich Panels—Theory and Experiment," NASA Technical Note No. TN D-5771.
[27] Grediac, M., 1993, "A Finite Element Study of the Transverse Shear in Honeycomb Cores," Int. J. Solids Struct., **30**(13), pp. 1777–1788.
[28] Gibson, L., and Ashby, F., 2001, *Cellular Solids: Structures and Properties*, Cambridge University Press, Cambridge, UK.
[29] Lorato, A., Innocenti, P., Scarpa, F., Alderson, A., Alderson, K. L., Zied, K. M., Ravirala, N., Miller, W., Smith, C. W., and Evans, K. E., 2009, "The Transverse Elastic Properties of Chiral Honeycombs," Compos. Sci. Technol., accepted.10.1016/j.compscitech.2009.07.008
[30] Abramovitch, H., Burgard, M., Edery-Azulay, L., Evans, K. E., Hoffmeister, M., Miller, W., Scarpa, F., Smith, C. W., and Tee, K. F., 2009, "Smart Tetrachiral and Hexachiral Honeycomb: Sensing and Impact Detection," Compos. Sci. Technol., accepted.10.1016/j.compscitech.2009.07.017